Curved passive mixing structures: a robust design to obtain efficient mixing and mass transfer in microfluidic channels

OPEN ACCESS
IOP Publishing
Journal of Micromechanics and Microengineering
J. Micromech. Microeng. **31** (2021) 015006 (13pp)
https://doi.org/10.1088/1361-6439/abc820

Curved passive mixing structures: a robust design to obtain efficient mixing and mass transfer in microfluidic channels

Ingrid H Oevreeide[1], Andreas Zoellner[2], Michal M Mielnik[3] and Bjørn T Stokke[1]

[1] Division of Biophysics and Medical Technology, Department of Physics, NTNU The Norwegian University of Science and Technology, NO-7491 Trondheim, Norway
[2] Palo Alto, CA, United States of America
[3] SINTEF ICT, MiNaLab Facility, Gaustadalléen 23C, 0373 Oslo, Norway

E-mail: bjorn.stokke@ntnu.no

Received 18 August 2020, revised 2 October 2020
Accepted for publication 5 November 2020
Published 2 December 2020

Abstract

Analyte mixing and delivery to a functionalized sensor surface are important to realize several advantages associated with biosensors integrated with microfluidic channels. Here, we present a comparison between a herringbone structure (HBS) and a curved passive mixing structure of their efficiency at facilitating mixing and surface saturation using fluorescein included in one of the inlets of a Y-channel microfluidic device. We performed a large parametric study to assess the effects of varying the height of the microfluidic channel as well as the height, width, and spacing of the passive mixing structures. Scanning confocal microscopy combined with a custom-designed image-analysis procedure were utilized to visualize and quantify the observed changes in efficiency in inducing solute mixing by the different designs. The flow patterns within the channels were found to vary significantly with changes in the geometry of the passive mixing structures, which in turn affected the efficiency of the channel at mixing the fluid and saturating the surface opposite the mixing structures. The solute mixing as a function of the channel length was also determined; an initial slow mixing rate does not always coincide with a low mixing index (MI). We found that the range of MIs for the curved mixing structure 1 cm downstream from the inlet was 0.85–0.99 whilst for our HBS it was 0.74–0.98, depending on the design parameters of the passive mixing structures. Overall, this study shows that the curved passive mixing structure family is more robust in inducing efficient mixing than the HBSs.

Supplementary material for this article is available online

Keywords: microfluidic mixing, curved passive mixing structures, confocal imaging, mixing efficiency, mixing distance

(Some figures may appear in color only in the online journal)

Abbreviations

HBS	Herringbone structure
CMS	Curved mixing structure
LOD	Limit of detection
MD	Mixing distance
MD_x	Mixing distance of value x

MI	Mixing index
MI_{CL}	Mixing index at the channel layers
MI_{SL}	Mixing index at the sensor layer
MI_y	Mixing index value of y
SGM	Slanted groove mixer
SHM	Staggered herringbone mixer
SPR	Surface plasmon resonance

List of symbols

A	Herringbone angle
A'	Perpendicular length resulting in angle change
$\bar{c}$	Mean pixel intensity
c_i	Pixel intensity
H_C	Channel height
H_{PM}	Passive mixing structure height
N	Number of pixels
S	Passive mixing structure spacing
W	Passive mixing structure width

1. Introduction

In recent decades, microfluidics has developed to be an increasingly important strategy within chemistry, biology and medicine due to miniaturization, versatility and the possibility of including a range of workflows [1–3]. This has led to the development of devices such as lab-on-chip [4], organ-on-chip [5], micro total-analysis systems [6], as well as diagnostic tools for medicine [7, 8], food and environmental controls. Selected applications of such designs include a sensor area functionalized with a capture moiety which requires interaction with a molecule to allow for a sensor response within the field of (bio) sensing. The merger of microfluidics with readout principles for biosensing yields devices with strongly enhanced performance due to miniaturization into the micro-regime, some of the benefits of which are increased reproducibility and efficiency, and reduced sample volumes, detection time, and limit of detection (LOD) [9]. Several of these advantages, such as reduced LOD, depend on the analyte–receptor moiety interaction. To be able to utilize these devices effectively, developing new designs to facilitate specific analyte–receptor moiety interactions can be critical in the fabrication of efficient diagnostic devices [10, 11].

Despite the clear advantages, this miniaturization comes with some challenges. Most evident is the drawback associated with the limitation of laminar flow occurring in channels at the micrometer length scale. Laminar flow occurs when the Reynolds (Re) number falls below 2000, resulting in diffusion being the driving mechanism for mixing. The mixing of fluids is therefore affected by the interface area and diffusion length between the fluids [12]. A traditional approach to achieve effective mixing at low Re numbers is to significantly increase the length of the microfluidic channels; however, this may not be favorable for certain devices. The limited mixing in the laminar flow regime has thus resulted in investigations focused on increasing the mixing efficiency within microfluidic channels.

Devices enhancing the mixing performance in microchannels can be divided into two main groups, active and passive mixers [13, 14]. An active mixer exploits external energy to drive the mixing process, and based on their nature, these can be categorized into four subgroups: magnetic, pressure, electric or sound field mixers. Examples of these mixing processes are magneto-hydrodynamic action [15], pulsing incoming flow rate [16], high-speed actuators [17], electrokinetic instabilities [18], piezoelectric actuators [19], electrohydrodynamic [20], dielectrophoretic [21], and acoustic chaotic advection [22]. Although the mixing efficiency of active mixers is often above 90% and they therefore on average offer an improvement in mixing compared to passive mixers [23], their associated increase in complexity, both in terms of fabrication and the need for peripherals in their operation, may limit their applications. Another challenge associated with active mixers, especially for biological and medical applications, is a potential temperature increase that can be harmful to biological molecules. For this reason, passive mixers are often preferred when designing microfluidic devices to be used for medical and biological purposes, as they rely solely on changes to the geometry of the channels, the mixing is driven by the fluid flow itself, and they seldom require peripherals to drive the mixing processes.

Passive mixers either mix via diffusion or chaotic flow; the two most common passive mixing designs exploiting diffusive mixing are the T- and Y-shaped micromixers. In these, the lateral transport of the mixing species drives the processes, eventually resulting in a homogenous solution, although the channel length necessary to achieve this outcome is typically unrealistically long for microdevices. The determination of the mixing performance of passive micromixers has therefore shifted to channels containing geometric variations and immersed structures. Examples of altered channel geometries include changing the direction of the channel such as zig-zag [24], spiral [25], split-and-recombine [26], and serpentine channels [27] adding obstruction in the channels [28] such as triangle baffles [29], J-shaped baffles [30], circular obstructions [31] or curved ribs [32], or changing the geometry on one or more of the channel surfaces. Currently the most studied example of this type of mixer is the staggered herringbone mixer (SHM), first introduced by Stroock *et al* [33]. They studied the effect on the mixing performance of chaotic micromixers caused by fabricated grooves in the ceiling of the microchannel. The effect of SHM and slanted groove mixer (SGM) pressure-driven flows was compared over a range of Re numbers, and it was found that their performance was ideal for low Re regimes [33, 34]. This increase in mixing efficiency was due to the formation of two helical flows, which increased the contact of the interface area between the flows, thus reducing the diffusion distance of the species and leading to a reduction in mixing time and channel distance [35–39]. After this initial introduction, the mixing performances of various designs based on the SGM and SHM have been reported. In the case of the SGM, this led to the barrier-embedded mixer [40–44] with grooves on the top and bottom of the channel [42, 45, 46], where the focus has been on changing the Re number or the geometric parameters to increase the mixing performance. Using a numerical approach, Tang *et al* [43] reported that the height and width of the channel and the

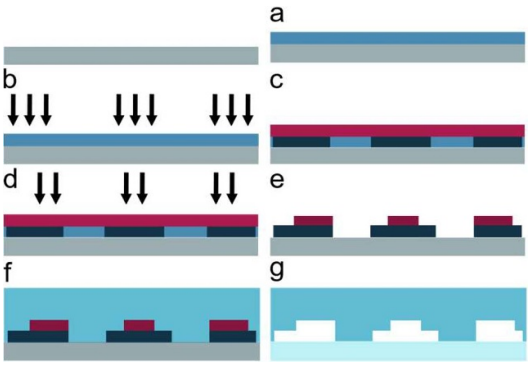

Figure 1. Schematic illustration of the two-layer lithographic-processing steps for the fabrication of microfluidic channels with passive mixing structures. (a) The negative photoresist was spun on the silicon wafer using a spin coater, followed by (b) exposure of the customized design to UV light using a maskless aligner. (c) The second resist layer was subsequently spun onto the first layer and (d) exposed to UV light. (e) The master mold for the soft lithography was then developed, silanized and (f) polydimethylsiloxane (PDMS) was cast on the master and cured. (g) The cured PDMS was peeled off from the master, the patterned PDMS side was exposed to oxygen plasma and bonded to a glass slide to prepare the sealed microfluidic device.

slanted grooves affect the rotation of the fluid and the mixing efficiency of the channel, where a reduced channel height facilitates fluid rotation. Similar studies on the SHM showed that the groove-height ratio and asymmetry had the largest effect on mixing efficiency, whereby an increase in groove height led to an increase in mixing efficiency [35, 47–49]. It was found that an asymmetry factor of two-thirds yielded the most efficient result [33], as the longer edge facilitated fluid transportation to the opposite side of the channel [49, 50]. It was also shown that an increase in groove width led to an increase in mixing performance [51, 52], whilst Cortes-Quiroz *et al* [53] also showed that the mixing efficiency depended on the channel height.

Most of the research currently conducted on passive mixers focuses on their capability of facilitating a homogeneous concentration of different fluidic species. However, passive mixers can also be used in conjunction with diagnostic devices and biosensors to enhance their overall efficiency [54, 55]. Recent works by Lynn *et al* showed how the geometry of the microfluidic channel influences the LOD of affinity-based biosensors. They studied the effect of chamber height on the sensitivity of an SPR-based biosensor and found an improvement in the LOD by a factor of four when the height was reduced from 47 μm to 7 μm [56]. Lynn *et al* also studied the use of an SGM, an SHM and a semi-loop passive mixing structure to analyze an increase in mass transfer to a sensor and a reduced impact of the depletion layer, and found an increase in binding rate when the sensor was located directly underneath a mixing structure [57]. They then increased the complexity of the channel by numerically introducing the SHM, and reported an increase in the efficiency of a planar biosensor surface through the use of the SHM, where the efficiency depended on the herringbone geometry as well as on the Péclet number [58]. Their subsequent experimental results showed an increase in sensor sensitivity using an SPR biosensor revealing an enhancement range of up to 400%, depending on SHM geometry, Péclet number and sensor length [59].

The studies of mixing performance in SHM structures mainly focus on the efficiency obtained at various channel lengths and including different structures. There is thus a need to map the development of the homogenization process as a function of the channel length and how the channel length is related to mass transport to the surface. In this study, we address the changes in mixing performance along the channel and compare the effects of several different geometric parameters, for two different passive mixers, on their ability to create a homogeneously distributed concentration of an initial step-function of a solute. We have designed a curved passive mixing structure [60], taking its inspiration from the parabolic flow profile that is present under pressure-driven flow and compared this to a herringbone mixer, whilst varying the channel height, and the height, depth, and spacing of the ceiling mixers. Furthermore, we analyzed the homogenization process in a domain opposite to the passive mixing structures, as an indication of the efficiency of transporting the fluorescent fluid to the surface of the channel.

2. Materials & methods

2.1. Fabrication

Microfluidic devices were fabricated using a two-layer photolithographic process (figure 1) to obtain the masters for the microfluidic channels with passive mixing structures in the ceiling. The lateral geometries of the channels were designed using appropriate software (CleWin) and the designs were used to pattern the photoresist in a maskless aligner (Heidelberg MLA150). A negative photoresist (MrDWL40, Micro Resist Technology) was spin coated on a 4 in. Si wafer and baked at 90 °C with a 5 °C min^{-1} ramp-up and ramp-down of temperature. The basic Y-channel design together with the alignment marks were then exposed at 405 nm using the MLA150 and post-exposure baked (PEB) at 90 °C following the same ramping procedure as previously described. Following patterning of the basic Y-channel in the first photoresist layer, the resist for layer two was spun onto layer one and baked at 90 °C with a 5 °C min^{-1} ramp-up and ramp-down of temperature. The mixer design was aligned and exposed, followed by the same PEB as that used for photoresist layer one. The master molds were obtained by developing the two-layer structure by immersing the Si-wafer in the developer (MrDev600, Micro Resist Technology) for 5–20 min, depending on the resist thickness.

The masters were then silanized with trichloro(1H, 1H, 2H, 2H-perfluoro-octyl)silane (Sigma Aldrich) using the vapor method. Following silanization, PDMS (Sylgard 184, Dow Corning) at a 10:1 (elastomer: curing agent) weight ratio was mixed and degassed. The PDMS was cast over the mold and cured at 65 °C for 3 h. The devices were then cut and peeled from the mold and the inlets and outlet were punched using a biopsy puncher (Ø1.0 mm, Miltex Biopsy Punch). The PDMS channels were directly bonded to microscope slides following

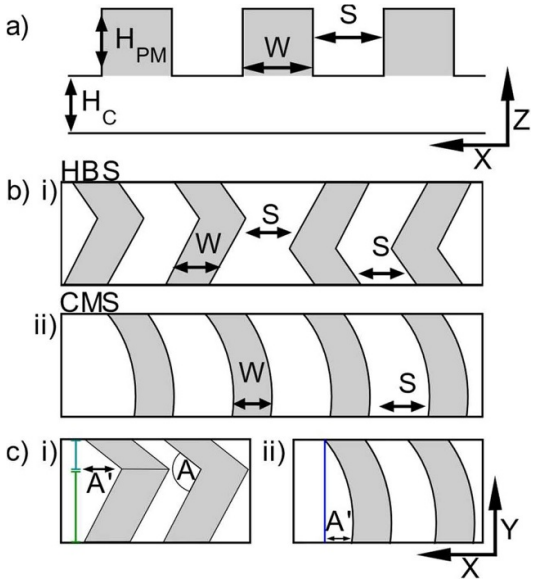

Figure 2. Arbitrary microfluidic channel designs showing the relevant parameters. (a) Side view of a channel design with passive mixing structures in the ceiling where the design parameters are as follows: H_c depicts the channel height; H_{PM} is the passive mixer height. Top view showing W and S depicting the passive mixer width and passive mixer spacing for (b) (i) HBS and (ii) CMS. A and A' depict the angle and intersection length for (c) (i) HBS where the length of the short arm up to the perpendicular intersection is 30 μm (teal line) and the length of the long arm is 70 μm (green line) and (ii) CMS where the blue line = 100 μm.

a 30 s oxygen plasma treatment (Diener Electronics), yielding the microfluidic devices to be characterized.

2.2. Passive mixer designs

Two different groups of passive mixing designs were studied. These groups were HBSs and CMSs. Sixteen different channels with passive mixing designs were fabricated for each of the two groups. The HBSs were divided into cycles of two structures, alternating the direction of the long and short arm for each cycle, whereas the CMSs were mono-directional. Due to the varying width and spacing of the structures, the number of structures per mixing length (1 cm) differed for each design.

The different designs were obtained by selecting different channel heights, and also the widths, spacings and heights of the structures. Straight microfluidic Y-channels without mixing structures with total heights of 20 μm and 40 μm were included as references to assess the mixing efficiency of the passive mixing structures.

The designs were realized on four different wafers, where the channel heights of the wafers were $H_C(W_1) = H_C(W_2) = 20\,\mu$m and $H_C(W_3) = H_C(W_4) = 40\,\mu$m. The selected design parameters for the width and the spacing between the structures, W and S, respectively, were related to the additional height of the passive mixer (H_{PM}). The H_{PM}:W:S:A' ratios were 1:1:1:1 for the first set of parameter design variables (PDVs), PDV 1. The same relations were 1:1:2:2; 1:2:2:2 and 1:2:4:4 for PDV 2, PDV 3 and PDV 4 respectively. For the HBS this resulted in a change in the angle (A) from 23° (W_1 PDV 1) to 130° (W_4 PDV 4). Considering the height ratio H_C:H_{PM}, this was 1:1 for W_1 and W_3, whilst for W_2 and W_4 it was 1:2 and 1:1.5, respectively. Table 1 shows an overview of the parametric values for the various designs.

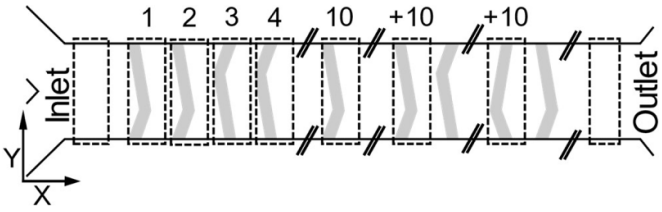

Figure 3. Illustration of locations of confocal image acquisition domains along a microfluidic channel from the inlet (left) to the outlet (right). An *XYZT*-stack was recorded for each of the first ten passive mixing structures. Following this, *XYZT* stacks were recorded at every tenth structure until the outlet was reached. For channels with fewer than 50 structures, images were acquired for every fifth structure.

2.3. Confocal imaging

The flow patterns in the dual-inlet microfluidic channels with various mixing structures in the ceiling were determined using confocal microscopy (Leica TCS SP5). Fluorescein sodium salt (Sigma–Aldrich) diluted in deionized (DI) water was imaged using a 10× (NA = 0.4) HC PL Apo CS dry objective. The fluorescein solution and DI H_2O were added to two separate 5 ml syringes and both were simultaneously introduced into the separate inlets of the Y-channel via plastic tubes at an injection rate of 10 μl min^{-1} using a syringe pump (Harvard apparatus), resulting in a total flow rate of 20 μl min^{-1} within the mixing channel.

For each chosen imaging location within the channel (figure 3), an *XYZT* stack was recorded, resulting in three Z-stacks per location. The pinhole was left at the optimal value resulting in an optical section thickness of 6.23 μm and a Z-level movement of 1.3 μm for each image acquisition. An argon laser and filters at 488 nm and 467 nm were used to simultaneously capture the fluorescence and the reflections in the channels as the Z-stack progressed. This characterization was conducted for 15–25 positions along the microfluidic channel to capture the efficiency of the passive mixing structures at affecting the flow behavior. Image acquisition was conducted from 60 min after starting the fluid flow to ensure a stationary state.

2.4. Data processing

The confocal *XYZT* stacks acquired along the microfluidic channel were analyzed using custom-designed MATLAB scripts. For each stack, a virtual sensor volume was chosen between two mixing structures, using the reflection mode to define the lowest and highest Z-level within the microfluidic channel. This contributed to analysis within the fluid adjacent

Table 1. Parametric values of the microfluidic channels with HBS and CMS in the ceiling of the PDMS channel. The table lists all combinations of the parameters implemented by the lithography process. The design parameters are schematically illustrated in figure 2. The master molds of the four wafers were realized for the fabrication of channels with total heights of: wafer 1(W_1) = 40 μm, wafer 2 (W_2) = 60 μm, wafer 3 (W_3) = 80 μm and wafer 4 (W_4) = 100 μm. Sixteen different channels were fabricated with design parameter variables for both the HBS and CMS, in addition to channels without mixing structures. All channels had a width (y-axis) of 100 μm, and a mixing channel length (x-axis) of 1 cm.

Channel height (H_C) μm	Passive mixer height (H_{PM}) μm	Parameter design variable (PDV) set	Width (W) μm	Spacing (S) μm	A′ = S μm
		1	**1 × H_{PM}** W_1: 20 W_2: 40 W_3: 40 W_4: 60	**1 × H_{PM}** W_1: 20 W_2: 40 W_3: 40 W_4: 60	**1 × H_{PM}** W_1: 20 W_2: 40 W_3: 40 W_4: 60
W_1: 20 W_2: 20 W_3: 40 W_4: 40	W_1: 20 W_2: 40 W_3: 40 W_4: 60	**2**	**1 × H_{PM}** W_1: 20 W_2: 40 W_3: 40 W_4: 60	**2 × H_{PM}** W_1: 40 W_2: 80 W_3: 80 W_4: 120	**2 × H_{PM}** W_1: 40 W_2: 80 W_3: 80 W_4: 120
		3	**2 × H_{PM}** W_1: 40 W_2: 80 W_3: 80 W_4: 120	**2 × H_{PM}** W_1: 40 W_2: 80 W_3: 80 W_4: 120	**2 × H_{PM}** W_1: 40 W_2: 80 W_3: 80 W_4: 120
		4	**2 × H_{PM}** W_1: 40 W_2: 80 W_3: 80 W_4: 120	**4 × H_{PM}** W_1: 80 = W_2: 160 W_3: 160 W_4: 240	**4 × H_{PM}** W_1: 80 W_2: 160 W_3: 160 W_4: 240

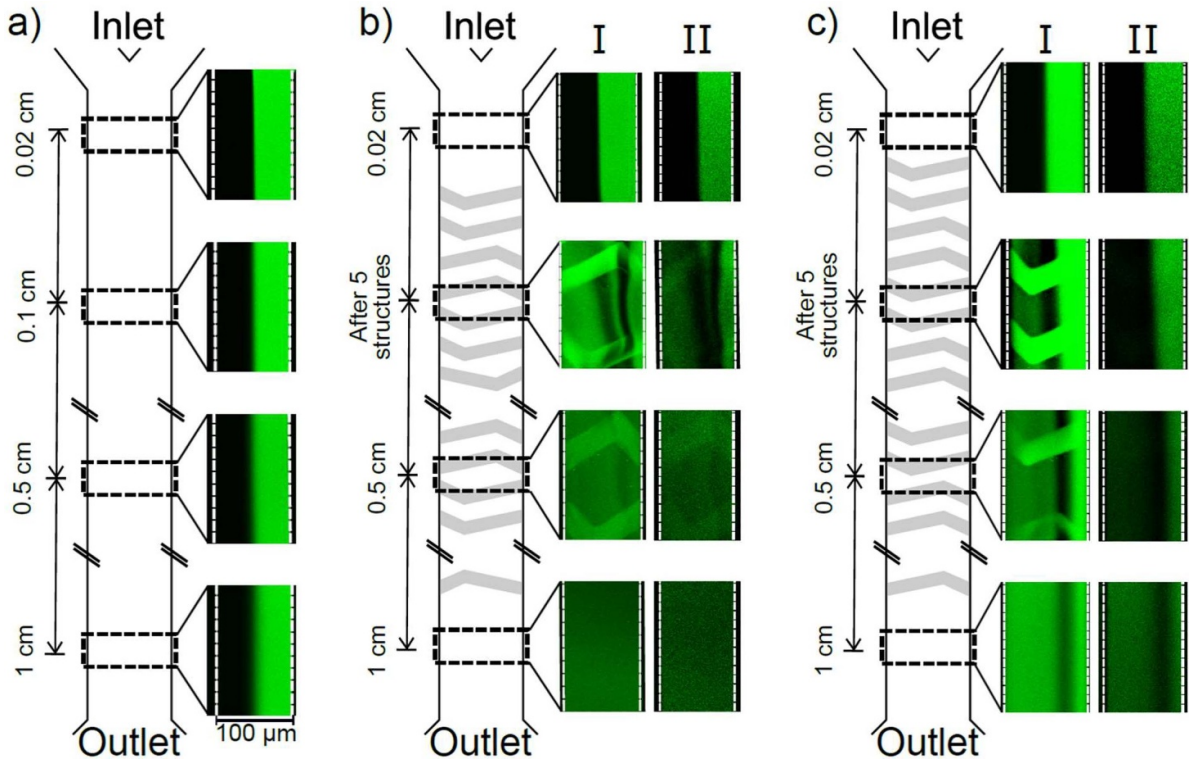

Figure 4. Confocal images of the distribution of the fluorophore as a function of channel length from the Y-channel inlet to the outlet for three microfluidic channels without a mixer and containing two different dimensions within the HBS design family: (a) 20 μm basic Y-channel, (b) W_2 with HBS 3 and (c) W_3 with HBS 2. The columns labeled I depict confocal micrographs representing all the Z-stack layers (AL) at the distance from the inlet of the channel as illustrated, and the columns labeled II depict confocal micrographs from the defined sensor layer (SL). The white dotted lines in the micrographs are the channel edges (walls). The direction of flow is from the inlet (top) to the outlet (bottom).

to the most likely location of a transducing sensor element, creating the fluid volumes used for mixing determination. After calculating the standard deviation at the inlet the pixel intensities were normalized to one, and each consecutive measurement for the same channel was then normalized to the inlet signal. We calculated the MI from the standard deviation of the normalized fluorescence intensity profile for each image volume using equation (1),

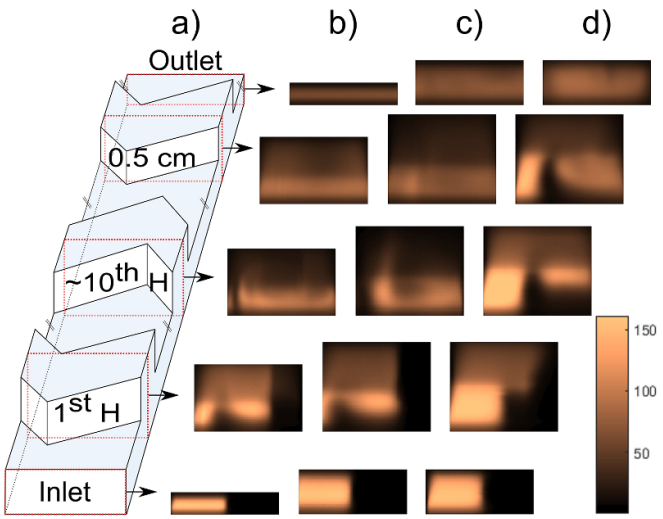

Figure 5. *YZ* visualization of the flow from the inlet to the outlet for three HBS designs. *XYZ* volume projected into one *YZ* slice; each pixel corresponds to the average along the *X*-axis. Pixel intensity from zero (no signal, water) to 160 (max signal from inlet).
(a) Schematic illustration of the channel with the HBS structures to aid in the location of the analysis. *YZ* cross-section visualizations rendered by MATLAB are depicted for (b) W_2 in HBS 3, (c) W_3 with HBS 4, and (d) W_3 with HBS 2. The scaling relationship between the channels is upheld.

$$MI = 1 - \frac{\sqrt{\frac{1}{N-1}\sum_{i=1}^{N}(c_i - \bar{c})^2}}{\sqrt{\frac{1}{N-1}\sum_{i=1}^{N}(c_i - \bar{c})^2}_{Inlet}} \quad (1)$$

where N is the number of pixels, c_i is the pixel intensity and $\bar{c}$ is the mean pixel intensity. A completely unmixed channel has an MI value of zero, whilst a completely mixed channel has a value of one, as $c_i = \bar{c}$. The MI, calculated as a function of the channel length, describes how efficiently the passive mixing structures induce hydrodynamic processes to enhance the mixing.

The MI was empirically observed to equilibrate towards the completely mixed state with increasing channel length. We found that a model consisting of a double exponential increase to saturation, using four parameters following equation (2):

$$MI = a\left(1 - e^{-bx}\right) + c\left(1 - e^{-dx}\right) \quad (2)$$

adequately described the development of the mixing indices downstream from the inlet (see supplementary information). Assessment of a minimal model required to account for the trend in MI(x) suggested a two-component exponential where *a, b, c* and *d* were all greater than zero, and $a + c < 1$, was adequate to account for the trends in MI(x), while at the same time limiting the number of parameters (figure S1 and table S1) (available online at https://stacks.iop.org/JMM/31/015006/mmedia). Thus, this approach was used for the analysis of MI(x).

3. Results and discussion

In the following, we present the visualization of the flow pattern of different HBSs and CMSs, and the impact of the geometric parameters within each family of passive mixing structures. This is followed by the determination of the MI along the channels for all the designs fabricated, based on both the overall fluorescence signal within the heights of the channel as well as the optical section near the defined area adjacent to the channel floor. The latter represents the evolution of the fluorescence distribution, mimicking the situation near a putative active sensing area e.g. as related to mass-transfer abilities.

3.1. Mixing visualization

3.1.1. Mixing via diffusion. The confocal images of the fluorescence concentration profile along the microfluidic channel (length = 1 cm, width = 100 μm and H_C = 20 μm) without a passive mixing structure (figure 4(a)) show the characteristic behavior for diffusion-driven mixing under laminar-flow conditions [61, 62]. The broadening of the concentration profile during the flow compares well with the diffusion distance of the fluoroprobe, calculated to 14 μm within a retention time of 60 ms from the inlet to the outlet, using a diffusion coefficient of 0.57 $\times$ 10^{-9} m^2 s^{-1} [63–65].

3.1.2. Microfluidic channel with herringbone mixer. The introduction of the commonly applied herringbone passive mixing structures, described in table 1 and figure 2, alleviates the challenges of limited mixing in the laminar flow regime of microfluidic channels. In the following, the results are presented for two sets of PDVs (table 1) used with HBS passive mixing structures (figure 4).

The *XY*-projected confocal images of all the *Z*-stack layers (AL) and the sensor layer (SL) for W_2 with HBS 3 (figure 4(b)) indicate that some blending has already taken place between the two sections after five structures, whereas a trend towards a more homogeneous state can be seen 0.5 cm from the inlet. The distribution of the fluorophore at the SL (figure 4(b) II) five periodic structures downstream from the inlet shows a larger lateral gradient than the AL-profiles (figure 4(b), I), whereas the distribution in the SL 0.5 cm downstream appears to be of a similar homogeneous state as the AL-profiles. This is in contrast to the change in distribution for the herringbone mixer W_3 with HBS 2 (figure 4(c)), where the trend in the developing fluorophore concentration distributions between the two design structures differs significantly. The mixing structures seem to be first flooded by fluorescence (as opposed to water), bringing the fluorescence to the opposite side of the channel, resulting in a shallow domain of low fluorophore concentration in the middle of the channel. Although the intensity becomes more homogenous after 0.5 cm, regions of low fluorescent intensity still remain in the concentration profile at the outlet (figure 4(c) I). A similar pattern was also experienced at the SL, where there were noticeable areas of low intensity at the same locations.

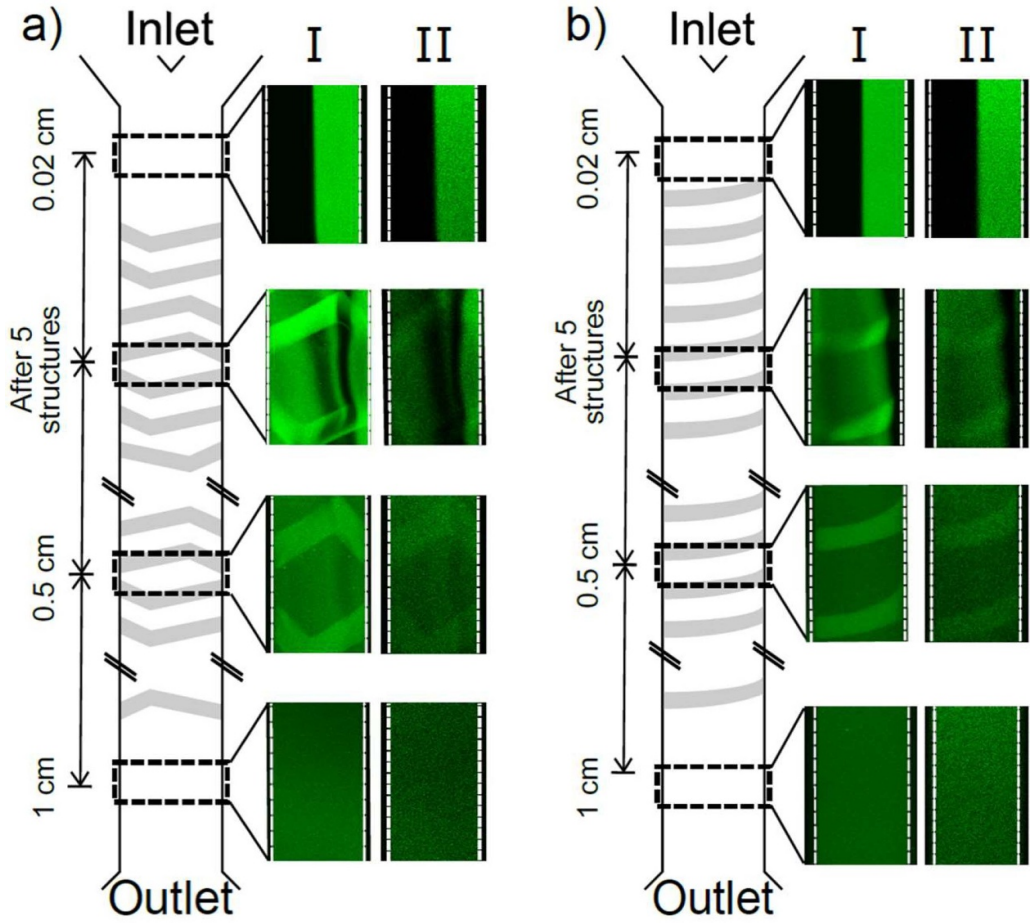

Figure 6. Confocal images of the distribution of the fluorophore as a function of the channel length from the Y-channel inlet to the outlet for two microfluidic channels (a) W_2 with HBS 3 and (b) W_2 with CMS 2. The columns labeled I depict confocal micrographs representing all the *Z*-stack layers (AL) at the distance from the inlet of the channel as illustrated, and the columns labeled II depict confocal micrographs from the defined sensor layer (SL). The white dotted lines in the micrographs are channel edges (walls). The direction of the flow is from the inlet (top) to the outlet (bottom).

It is clear from the outlet images in figure 4 that both mixing channels performed much better than the standard Y-channel (figure 4(a)), where mixing only occurs via diffusion. Both W_2 with HBS 3 (figure 4(b)) and W_3 with HBS 2 (figure 4(c)) increase the mixing capabilities of the channel, although it can be seen that the extent of the mixing depends on the PDV of the HBS.

As the mixing in these channels does not solely occur in the lateral direction of the channel, across the *Y*-axis, the flow pattern in the *YZ* projection has been investigated (figure 5). This allows for a deeper understanding of the processes that occur as the fluid flow is perturbed by the passive mixing structures.

The projection of the fluorescent intensity along a limited length in *X* yielding a *YZ* projection at various stages along the microfluidic channels (figure 5) can be combined with the *XY* projection (figure 4) to provide more comprehensive information about the mixing development. Specifically, figures 5(b) and (d) provide complementary information to the *YX* projections in figures 4(b) and (c), respectively.

The flow pattern along the channel is quite similar for W_2 with HBS 3 (figure 5(b)) and W_3 with HBS 4 (figure 5(c)), compared to that visualized for W_3 with HBS 2 (figure 5(d)). The change in the initial flow pattern from the inlet via the first passive mixing structure (image 2) for the channels W_2 with HBS 3 and W_3 with HBS 4 shows a relocation of the highest fluorescence from the left side of the channel towards the middle, with a narrower fluorescence-depleted domain indicative of an unlabeled water stream observed on the left side of the channel. After ten structures, most of the channel provides a clear fluorescent signal; however, a water band remains near the left wall of the channel (figure 5(b)), and a similar distribution is seen for W_3 with HBS 4 (figure 5(c)). Due to the increase in height of W_3 with HBS 4, it can be seen that the flow is rotating, as there is a slight curved area of low intensity in the middle of the channel. After 0.5 cm ($MD_{0.5}$), a relatively homogeneous distribution was observed within the channel, which remains the case until the outlet. This is in good agreement with what was seen in the confocal images in figure 4(b).

In comparison, the distribution of the fluorescent intensity for W_3 with HBS 2 (figure 5(d)) suggests that the initial state is dominant after the first structure (e.g. about 50% coverage), but there is some fluorescence throughout the grooves in the

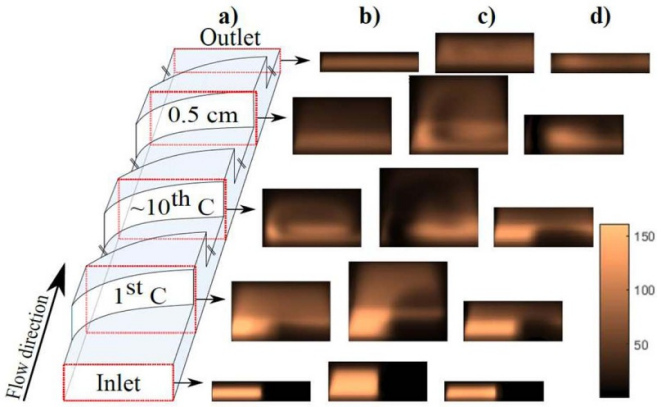

Figure 7. *YZ* visualization of the flow from the inlet to the outlet for three CMS designs. (a) Schematic illustration of the channel with the curved structures to aid in the location of the analysis. The *YZ* cross-section visualizations from the confocal images are depicted for (b) W_2 with CMS 2, (c) W_3 with CMS 3, and (d) W_1 with the CMS 1 mixer designs. The scaling relationship between the channels is upheld. The *XYZ* volume is Ccompressed into one *YZ* slice; each pixel corresponds to the average along the channel. Pixel intensity from zero (no signal) to 160 (maximum signal from inlet).

mixing structure. After ten structures there is a signal at the top and this is the case for all the mixing structures, although the situation where there is no fluorescence at the left surface of the channel persists. The fluid is observed turning from the left half over into the right half which is further exemplified for the projection after 0.5 cm of the channel length, where it is seen that the fluid has now completed at least one full rotation, although a stream of water continues to pass through the channel (figure 5(d), the image at 0.5 cm). Although W_3 with HBS 2 shows a signal on the left of the channel in figures 4(c), 5(d) shows that the signal is located at the top of the channel, making it less preferred for use in conjunction with surface sensors. The distribution of fluorescence at the surface for W_2 with HBS 3 and W_3 with HBS 4 requires less than ten structures for high surface coverage, although a heterogeneous environment still persists within the channel, as opposed to W_3 with HBS 2 which, even after 0.5 cm of mixing, does not result in a matching surface distribution or a mixed state.

3.1.3. Microfluidic channel with curved passive mixer. In comparison to the HBS designs, we analyzed the mixing performance of a novel CMS design implemented based on inspiration from the parabolic flow profile under pressure-driven flow. The design parameters of these curved structures follow the same ratios as those implemented for the HBS (figure 2, table 1).

The microfluidic channels with the HBS and CMS structures that yielded the most efficient mixing enhancement were chosen as examples for the comparison of the confocal flow visualizations form a basis for possible differences in the flow patterns induced by these geometries. The *XY* projection of the flows in channels with a CMS as compared to an HBS (figure 6) indicates that the main difference in mixing between these designs occurs within the first few structures. The flow in the microchannel with the CMS does not yield a fluorescence-depleted region in the middle of the channel, as occurs with the HBS design. A nearly homogeneous fluorescence distribution is observed in the channel after five repeats of the CMS; nevertheless, a fluorescence-depleted stream is observed at the right-hand side of the channel. There is also a domain of higher intensity to the left of the channel, which is the opposite of the signal seen at the inlet. These observations indicate that the CMS rotates the flow, and a similar trend is also visible at the SL. The *XY* projections of the flow are similar for the AL and SL cases from 0.5 cm and the solutions appear completely mixed from this point onwards.

The *YZ* projections at various stages along the microfluidic channels (figure 7) for three microfluidic channels using the CMS design with different parameter values provide complementary information regarding the mixing process.

The *YZ* projection for the flow in the channel with W_2 with CMS 2 (figure 7(b)) shows that a large part of the channel and mixing structure is already flooded by fluorescence after one structure, although the majority of the fluorescence is still located in the left part of the channel. The flow rotates in a clockwise manner via the passive mixer, which was further evident after ten structures where fluorescence was observed at both walls of the channel. Additionally, a circular domain depleted of fluorescence was observed on the left-hand side, indicating a spiral pattern. The *YZ* projection indicates a change in the fluorescent distribution from the left at the inlet to the right, with a turning stream of water clearly going from the bottom right-hand side, up on the left side and over towards the right side again.

Overall, the projections convey information about flow patterns developing along the channels of the various CMSs that are quite similar to each other (figure 7), although the rate at which mixing occurs varies drastically between the different PDVs implemented. From the change in fluorescence distributions observed, W_2 with CMS 2 should be the most efficient channel in inducing mixing, as a homogeneous environment can be observed after 0.5 cm. This does not occur until after 0.5 cm for W_3 with CMS 3 (figure 7(c)), whilst W_1 with CMS 1 (figure 7(d)) does not reach a homogeneous state within 1 cm of mixing.

3.2. Mixing efficiency

While the projections of the fluorophore concentrations provide details about flow patterns and their differences along channels with different mixing structures, for different design families and parameters within these families, the approach is too detailed for a quantitative comparison of mixing efficiency. In the following, estimates of the MI along the mixing channel for the various microfluidic channels are described. This was done for the channel layers (CLs) which correspond to the volume defined in section 2.4 and the SL, defined as the first *Z*-level of the *Z*-stack included in the CL. The results of the MI are grouped based on the PDV sets (table 1), where distinct heights of the fluidic channel (H_C) and the mixing structures (H_{PM}) are specific to each wafer, and the presentation is therefore based on this. The typical difference between these

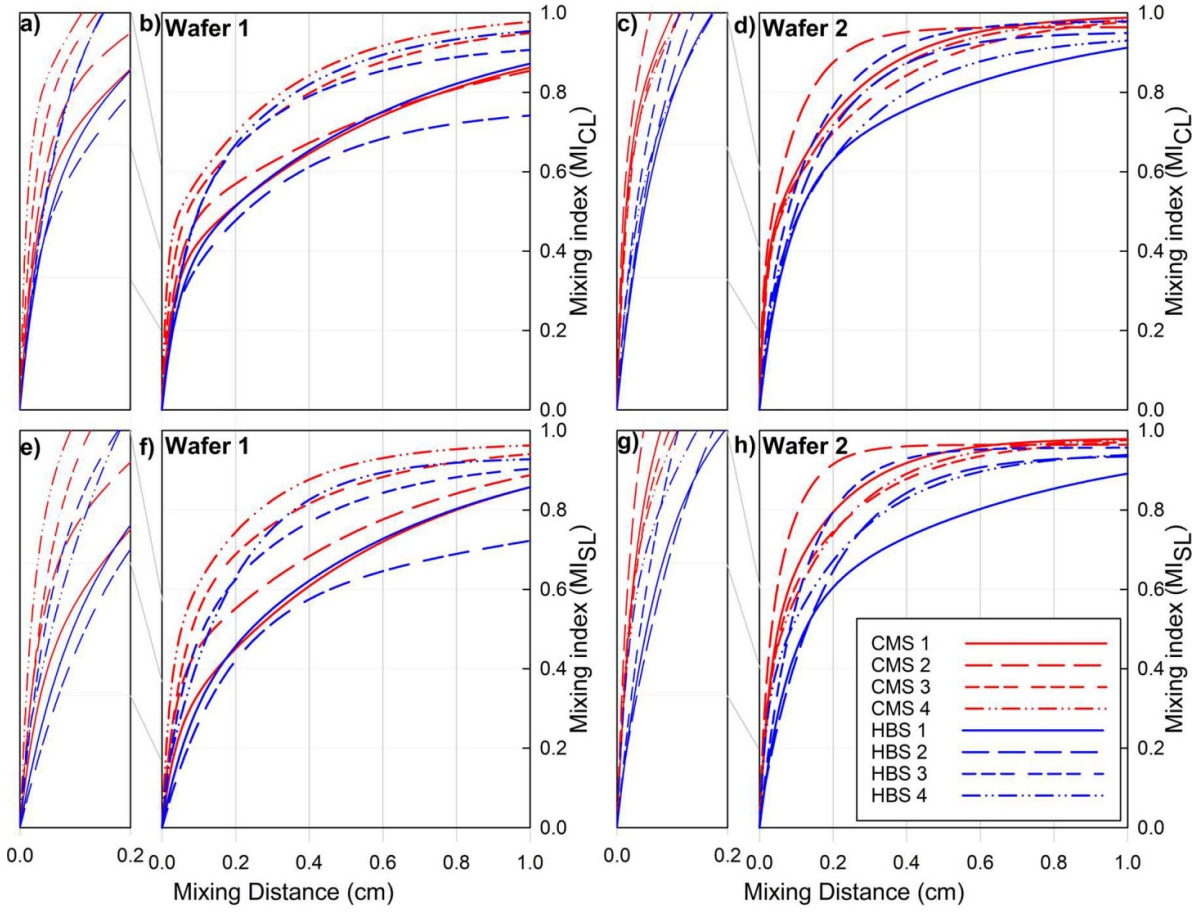

Figure 8. Mixing index at the channel layers versus the channel length from the double exponential model (b), (d), (f), (h), with an enlarged version of the initial 0.2 cm up to $MI_{0.6}$ (a), (c), (e), (f). Channels with HBS (blue) and CMS (red) passive mixing structures for channels made using (a), (b) wafer 1, (c), (d) wafer 2, for the channel layers (CLs) and (e), (f) wafer 1, and (g), (h) wafer 2 for the sensor layer (SL). The data obtained for channels with passive mixing structures in the two design families with sets of parameter design variables (PDV sets, table 1) are depicted as follows: PDV set 1 is represented by a solid line, PDV set 2 by a long dashes , PDV set 3 by three short dashes and PDV set 4 by dash-dot-dot.

model fits and the experimentally determined MI at a particular location is of the order of 2%–2.5% (table S1).

For the various channels fabricated based on masters from wafer 1 (W_1), it is observed that differences in the MI(x) depend more on the set of PDVs selected than whether the mixing design is in the HBS or CMS family (figure 8). The MI observed both for PDV sets 1 and 2 develops less strongly with channel length as compared to PDV sets 3 and 4 for both HBS and CMS. Furthermore, the MIs increase faster along the channel for the CMSs than the HBSs for each PDV set. The initial increase in MI (figure 8(a)) clearly shows that the CMS yields a much faster initial increase in the amount of mixing, with PDV sets 3 and 4 reaching $MI_{0.6}$ at 0.15 cm downstream in the channel. There is a large spread in the mixing efficiencies reached at the outlet, with MIs ranging from 0.74 (W_1 with HBS 2) to 0.95 (W_1 with CMS 4), yielding an overall difference of 0.21. The four channels reaching $MI_{0.6}$ within the first 0.2 cm of the channel correspond to the channels yielding the highest MI at the outlet. For the various designs fabricated based on W_1 (table 1), the observed differences in MI_{SL} (figure 8(f)) resemble those observed for MI_{CL} (figure 8(b)), where the development of MI_{SL} depends more strongly on the PDV set than on the two design families, HBS or CMS. The initial increase in MI_{SL} (figure 8(e)) clearly shows that the CMS yields faster surface coverage when comparing the PDV sets. Comparing the initial MI_{SL} (figure 8(e)) to MI_{CL} (figure 8(a)), the majority of the channels show a slower development over the MD.

For wafer 2 (W_2), all channels reach $MI_{0.9}$ or more at the outlet (figure 8(d)). Within the designs for W_2, there is a tendency for the CMS to yield a larger MI throughout the whole channel length than the HBS structures, except for HBS 3, while HBS 1 resulted in the lowest MI of 0.91.

The initial increase in MI showed that all channels reached $MI_{0.6}$ within the first 0.2 cm downstream of the channel inlet (figure 8(c)). However, the CMS yielded a more efficient increase in the initial MI than the HBS designs, where W_2 with CMS 2 was the only design to reach $MI_{0.8}$ in less than 0.2 cm.

The developments of MI_{SL} (figure 8(h)) along the MD correspond well with those observed in figure 8(d). At the outlet, the CMS outperforms the HBS in all cases, with the

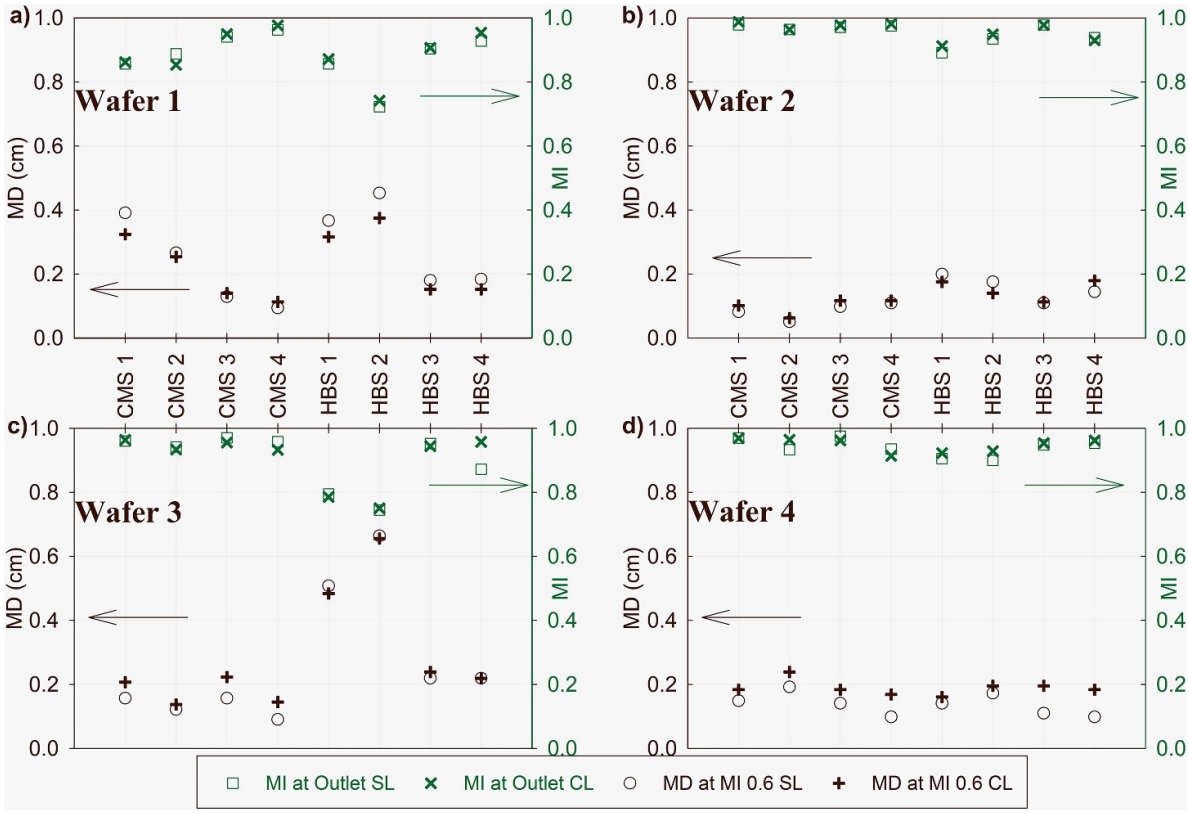

Figure 9. Mixing distance to achieve a 0.6 (60%) mixing index (left *y*-axis, black) for the channel layers (black +) and the sensor layer (black ◯) and the mixing index at the outlet (right *y*-axis, green) for the channel layers (green ×) and the sensor layer (green □) for the microfluidic channels with passive mixing structures, as indicated. The parameter values for microfluidic channels with mixing structures as defined by the parameter design variable sets in table 1 were used in the preparation of (a) wafer 1, (b) wafer 2, (c) wafer 3 and (d) wafer 4, respectively.

spread of MI_{SL} values being within 0.01. Although the CMS outperforms the HBS in this instance, all the channels reach a value above $MI_{0.9}$ at the outlet. The initial increase in MI_{SL} (figure 8(g)) also showed that each design reached $MI_{0.6}$ within the first 0.2 cm of the mixing channel and are therefore efficient in delivering the 'analyte' to the channel surface in a short distance.

The majority of the channels experience a decrease in the mixing rate over the MD of 1 cm, with noticeable exceptions from the HBS family (W_1 with HBS 2, W_2 with HBS 1, W_3 with HBSs 1 and 2). The remaining channels approach the maximum mixing value and a 1 cm mixing channel would be sufficient to realize their potential. The MI(x) data for the channels with the HBS and CMS fabricated on wafer 3 (W_3) and wafer 4 (W_4) are presented in figure S2.

For an overall performance indicator, we employ the MI values reached at the outlet, as well as the MD values necessary to reach $MI_{0.6}$ for all channels, to provide a comparison of the various passive mixing designs (figure 9).

There is a strong correlation between the MD for $MI_{0.6}$ to the MI at the outlet, where a lower MD corresponds to a shorter distance needed to achieve 60% mixing in the channel (figure 9). Channels fabricated on W_1 and W_3 exhibit the largest difference between HBS and CMS. The main outliers result in less efficient mixing such as W_2 with HBS 1, W_3 with HBS 1 and 2. From these, we can see that increasing the width (W) of the structure increases the mixing and mass-transfer ability of the channel. This was also observed with an increase in the spacing between the structures. It can be seen that an increasing H_C:H_{PM} ratio results in an overall increase in MI, regardless of the PDV set used. From this, two trends stand out, one being the H_C:H_{PM} ratio and the second is that the lowest efficiencies found are for the HBS designs, in particular for W_1 and W_3 with PDV sets 1 and 2.

The observed effect of H_C:H_{PM} on the MI (1 cm) and $MI_{0.6}$ is highly significant: channels with mixing structures using W_2 and W_4 yield the most efficient channels with the least spread in MI, where W_2 has a 1:2 (H_C:H_{PM}) ratio and W_4 has a 1:1.5 ratio, compared to W_1 and W_3 which both have a 1:1 ratio. This increase in MI with an increasing mixer depth ratio coincides well with previous studies, although the majority of cases had a height ratio below 1 [49, 51, 53].

From the literature, one would expect PDV sets 3 and 4 to perform better than PDV sets 1 and 2, due to the increase in structure width (W), as a wider mixer leads to an increase in surface interactions [66]. The current data for the HBS design are in line with this (figure 9). However, no such trend was found for the CMS design, suggesting that the flow pattern adopted varies from that of the HBS design, which is supported by our results (section 3.1).

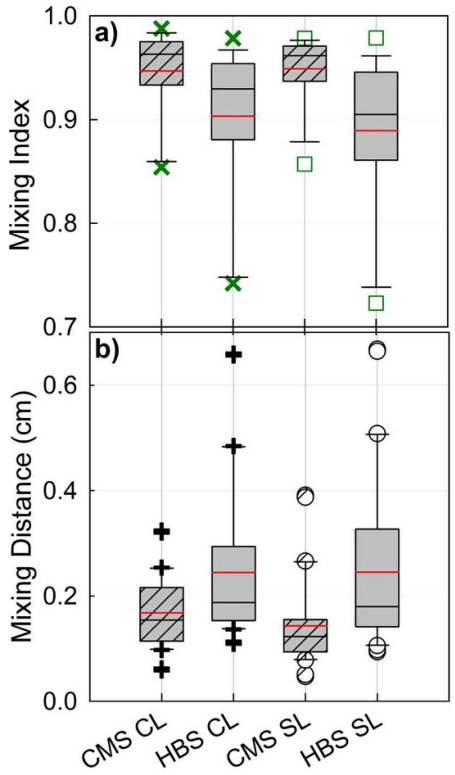

Figure 10. Boxplots depicting the (a) range of mixing indices at the outlet and (b) the mixing distance required to reach $MI_{0.6}$ for the CMS and HBS designs in the channel (CL) and at the sensor layer (SL). The black plus and the white circle (+, ◯) represent the MDs for $MI_{0.6}$ for the CL and the SL, respectively. The green cross and the white square (×, □) represent the MIs at the outlet for the CL and the SL respectively. The mean is the red line and the median is the black line within each box. The box corresponds to the interquartile range (50% of the data), whilst the lines (⊤ ⊥) represent 1.5× the interquartile range.

It was found that the CMS had a more robust reaction to the changing parameters, both for mixing efficiency within the channel as well as mass transfer to the SL. From figure 10 it can be seen that the CMS had a minimum mixing efficiency of 0.85 (CMS CL) compared to 0.72 (HBS SL) for the HBS. The median values for the CMS designs were above 0.95 for both CL and SL, whereas this was reduced to ∼0.92 for the HBS design. The range of MIs for the HBS designs was observed to be twice that observed for the CMS (tables S2 and S3).

The data reported here compare well to other studies reporting a change of MI downstream from the inlet using passive mixing structures. Examples of this include the reported increase of MI to nearly 0.4 at an MD of 2.2 mm from flow simulations at Re = 0.267 for either square wave, zig-zag or curved channel designs [67]. Increasing the Re initially yielded a less efficient increase in mixing using these designs, followed by increased efficiency. The estimated MDs required to obtain an MI of 0.6 based on those reported designs are on the order of 0.33–0.36 cm (Re = 0.267) and about 1 cm (Re = 20), indicating a much poorer mixing performance as compared to the CMS structures (figure 10) introduced here. The recently reported comparison of the performance of various passive micromixer designs by Kim *et al* [68] indicated that various designs yielded optimal mixing performance, depending on the Reynolds number. The most realistic comparison would be to barrier-embedded micromixers [41], which showed a maximum MI of 0.401 after 21 mm (Re = 120); at Re = 1 this was reduced to 0.226. Comparing this with other passive mixers at Re = 1, the two-layer serpentine-crossing micromixer showed the most efficient mixing at MI 0.915. A further facet of the present study is a possible development route that combines the passive mixing structures with a sensor integrated into the floor of the microfluidic channel. Some of the passive mixing structures used in the comparison here would appear to support a combination with sensing elements.

4. Conclusions

We have performed a large parametric study comparing the MI progression along microfluidic channels within two families of passive mixing ceiling structures, the HBS and a CMS, varying several different geometric parameters within each family. The MI was determined for the channel and the surface layer of the channel opposite the location of the mixing structures, providing information as to the mixing efficiency and their ability to saturate the channel surface. We utilized confocal microscopy to visualize the distribution of a fluorescent marker injected into one of the Y-channel inlets at 15–25 different positions along the channel, allowing for the progression of the downstream mixing of the flow to be determined.

The CMS generally provides a much faster transition towards a homogeneous solute distribution, compared to the HBS design; the mixing length to achieve $MI_{0.6}$ is, in many cases, less than 0.1 cm. Among the CMSs, the ones with a groove height (H_{PM}) relative to the channel height (H_C) H_{PM}:H_C = 2:1 (wafer 2) and a spacing (S) relative to the groove width (W) and height S:W:H_{PM} = 2:1:1 (PDV 2) yield the most rapid increase in MI downstream from the inlet. Although a similar development of solute homogenization was observed in the SL as compared to the average of all CLs, a direct correspondence between these analysis parameters for a specific mixing design does not always exist. The mass transfer efficiencies are affected by the geometry of the channels. As with the channel mixing, W_4 and W_2 provide the most homogenous results.

The range of the MI observed 1 cm downstream from the inlet is found to be 0.99 to 0.85 (0.14) for the CMS family, whilst for HBS it is 0.98 to 0.74 (0.24). For this experimental study, the channel which showed the maximum MI at the outlet was W2 with CMS 1 (MI = 0.99) and the most rapid design was W2 with CMS 2, reaching $MI_{0.6}$ in 0.063 cm. It is evident from these results that there is a larger chance of designing a mixing channel with an efficiency of over 90% using the CMS design.

It is also interesting to note that rapid initial mixing does not necessarily result in the largest MI values at the outlet. Care should therefore be taken when choosing a mixer design, considering the importance these different rates would have on

the integration of the mixer with with a biosensor. Out of the current mixing structures studied, the W_2 with CMS 2 outperforms all the other designs and should therefore be considered as a possible passive mixing design for microfluidic mixers requiring rapid and near-complete mixing in this flow regime.

Acknowledgments

This work was supported by the Research Council of Norway within the Lab-on-a-Chip Biophotonic Sensor Platform for Diagnostics, contract 248869/O70. The project is part of Center for Digital Life Norway and is also supported by the Research Council of Norway, Grant No. 248810. The Research Council of Norway is acknowledged for the support to the Norwegian Micro- and Nano-Fabrication Facility, NorFab, project number 245963/F50.

ORCID iDs

Ingrid H Oevreeide https://orcid.org/0000-0002-7240-3568
Bjørn T Stokke https://orcid.org/0000-0003-2991-8088

References

[1] Convery N and Gadegaard N 2019 30 years of microfluidics *Micro Nano Eng.* **2** 76–91
[2] Ding Y, Howes P D and Demello A J 2020 Recent advances in droplet microfluidics *Anal. Chem.* **92** 132–49
[3] Kong T, Shum H C and Weitz D A 2020 The fourth decade of microfluidics *Small* **16** 2000070
[4] Temiz Y, Lovchik R D, Kaigala G V and Delamarche E 2015 Lab-on-a-chip devices: how to close and plug the lab? *Microelectron. Eng.* **132** 156–75
[5] Kimura H, Sakai Y and Fujii T 2018 Organ/body-on-a-chip based on microfluidic technology for drug discovery *Drug Metab. Pharmacokinet.* **33** 43–48
[6] Lee S J and Lee S Y 2004 Micro total analysis system (μ-TAS) in biotechnology *Appl. Microbiol. Biotechnol.* **64** 289–99
[7] Masson J F 2017 Surface plasmon resonance clinical biosensors for medical diagnostics *ACS Sens.* **2** 16–30
[8] Chen Z *et al* 2020 Rapid and sensitive detection of anti-SARS-CoV-2 IgG, using lanthanide-doped nanoparticles-based lateral flow immunoassay *Anal. Chem.* **92** 7226–31
[9] Arlett J L, Myers E B and Roukes M L 2011 Comparative advantages of mechanical biosensors *Nat. Nanotechnol.* **6** 203–15
[10] Lynn N S, Špringer T, Slabý J, Špačková B, Gráfová M, Ermini M L and Homola J 2019 Analyte transport to micro-and nano-plasmonic structures *Lab Chip* **19** 4117–27
[11] Squires T M, Messinger R J and Manalis S R 2008 Making it stick: convection, reaction and diffusion in surface-based biosensors *Nat. Biotechnol.* **26** 417–26
[12] Ottino J M and Wiggins S 2004 Introduction: mixing in microfluidics *Philos. Trans. R. Soc.* A **362** 923–35
[13] Nguyen N T and Wu Z 2005 Micromixers—a review *J. Micromech. Microeng.* **15** R1–16
[14] Ward K and Fan Z H 2015 Mixing in microfluidic devices and enhancement methods *J. Micromech. Microeng.* **25** 094001
[15] West J, Karamata B, Lillis B, Gleeson J P, Alderman J, Collins J K, Lane W, Mathewson A and Berney H 2002 Application of magnetohydrodynamic actuation to continuous flow chemistry *Lab Chip* **2** 224–30
[16] Glasgow I and Aubry N 2003 Enhancement of microfluidic mixing using time pulsing *Lab Chip* **3** 114–20
[17] Shang X, Huang X and Yang C 2016 Vortex generation and control in a microfluidic chamber with actuations *Phys. Fluids* **28** 122001
[18] Oddy M H, Santiago J G and Mikkelsen J C 2001 Electrokinetic instability micromixing *Anal. Chem.* **73** 5822–32
[19] Takayama T, Miyashiro H, Tsai C-H D, Ito H and Kaneko M 2018 On-chip density mixer enhanced by air chamber *Biomicrofluidics* **12** 044108
[20] El Moctar A O, Aubry N and Batton J 2003 Electro-hydrodynamic micro-fluidic mixer *Lab Chip* **3** 273–80
[21] Salmanzadeh A, Shafiee H, Davalos R V and Stremler M A 2011 Microfluidic mixing using contactless dielectrophoresis *Electrophoresis* **32** 2569–78
[22] Frommelt T, Kostur M, Wenzel-Schäfer M, Talkner P, Hänggi P and Wixforth A 2008 Microfluidic mixing via acoustically driven chaotic advection *Phys. Rev. Lett.* **100** 034502
[23] Cai G, Xue L, Zhang H and Lin J 2017 A review on micromixers *Micromachines* **8** 274
[24] Tsai C-H D and Lin X-Y 2019 Experimental study on microfluidic mixing with different zigzag angles *Micromachines* **10** 583
[25] Vatankhah P and Shamloo A 2018 Parametric study on mixing process in an in-plane spiral micromixer utilizing chaotic advection *Anal. Chim. Acta* **1022** 96–105
[26] Wang X, Liu Z, Wang B and Song Q 2020 Investigations into planar splitting and recombining micromixers with asymmetric structures *J. Micromech. Microeng.* **30** 015006
[27] Chen X, Li T, Zeng H, Hu Z and Fu B 2016 Numerical and experimental investigation on micromixers with serpentine microchannels *Int. J. Heat Mass Transf.* **98** 131–40
[28] Bhagat A A S, Peterson E T K and Papautsky I 2007 A passive planar micromixer with obstructions for mixing at low Reynolds numbers *J. Micromech. Microeng.* **17** 1017–24
[29] Wang L, Ma S, Wang X, Bi H and Han X 2014 Mixing enhancement of a passive microfluidic mixer containing triangle baffles *Asia-Pacific J. Chem. Eng.* **9** 877–85
[30] Lin Y C, Chung Y C and Wu C Y 2007 Mixing enhancement of the passive microfluidic mixer with J-shaped baffles in the tee channel *Biomed. Microdevices* **9** 215–21
[31] Alam A, Afzal A and Kim K Y 2014 Mixing performance of a planar micromixer with circular obstructions in a curved microchannel *Chem. Eng. Res. Des.* **92** 423–34
[32] Borgohain P, Arumughan J, Dalal A and Natarajan G 2018 Design and performance of a three-dimensional micromixer with curved ribs *Chem. Eng. Res. Des.* **136** 761–75
[33] Stroock A D, Dertinger S K W, Ajdari A, Mezić I, Stone H A and Whitesides G M 2002 Chaotic mixer for microchannels *Science* **295** 647–51
[34] Stroock A D, Dertinger S K, Whitesides G M and Ajdari A 2002 Patterning flows using grooved surfaces *Anal. Chem.* **74** 5306–12
[35] Hassell D G and Zimmerman W B 2006 Investigation of the convective motion through a staggered herringbone micromixer at low Reynolds number flow *Chem. Eng. Sci.* **61** 2977–85
[36] Kee S P and Gavriilidis A 2008 Design and characterisation of the staggered herringbone mixer *Chem. Eng. J.* **142** 109–21
[37] Kirtland J D, McGraw G J and Stroock A D 2006 Mass transfer to reactive boundaries from steady three-dimensional flows in microchannels *Phys. Fluids* **18** 073602
[38] Lynn N S and Dandy D S 2007 Geometrical optimization of helical flow in grooved micromixers *Lab Chip* **7** 580–7

[39] Aubin J, Fletcher D F, Bertrand J and Xuereb C 2003 Characterization of the mixing quality in micromixers *Chem. Eng. Technol.* **26** 1262–70
[40] Kang T G, Singh M K, Kwon T H and Anderson P D 2008 Chaotic mixing using periodic and aperiodic sequences of mixing protocols in a micromixer *Microfluid. Nanofluid.* **4** 589–99
[41] Kim D S, Lee S W, Kwon T H and Lee S S 2004 A barrier embedded chaotic micromixer *J. Micromech. Microeng.* **14** 798–805
[42] Meijer H E H, Singh M K, Kang T G, Jmj D T and Anderson P D 2009 Passive and active mixing in microfluidic devices *Macromol. Symp.* **279** 201–9
[43] Tang Y, Wu J, Czyzewska E and Stanley K 2004 An optimized micromixer with patterned grooves *Proc.—2004 Int. Conf. on MEMS, NANO and Smart Systems, ICMENS 2004* pp 300–5
[44] Kang T G and Kwon T H 2004 Colored particle tracking method for mixing analysis of chaotic micromixers *J. Micromech. Microeng.* **14** 891–9
[45] Howell P B, Mott D R, Fertig S, Kaplan C R, Golden J P, Oran E S and Ligler F S 2005 A microfluidic mixer with grooves placed on the top and bottom of the channel *Lab Chip* **5** 524–30
[46] Singh M K, Kang T G, Meijer H E H and Anderson P D 2008 The mapping method as a toolbox to analyze, design, and optimize micromixers *Microfluid. Nanofluid.* **5** 313–25
[47] Ansari M A and Kim K Y 2007 Shape optimization of a micromixer with staggered herringbone groove *Chem. Eng. Sci.* **62** 6687–95
[48] Hossain S, Husain A and Kim K Y 2010 Shape optimization of a micromixer with staggered-herringbone grooves patterned on opposite walls *Chem. Eng. J.* **162** 730–7
[49] Yang J T, Huang K J and Lin Y C 2005 Geometric effects on fluid mixing in passive grooved micromixers *Lab Chip* **5** 1140–7
[50] Vasilakis N, Moschou D and Prodromakis T 2016 Computationally efficient concentration-based model for accurate evaluation of T-junction inlet staggered herringbone micromixers *Micro Nano Lett.* **11** 236–9
[51] Aubin J, Fletcher D F and Xuereb C 2005 Design of micromixers using CFD modelling *Chem. Eng. Sci.* **60** 2503–16
[52] Cortes-Quiroz C A, Zangeneh M and Goto A 2009 On multi-objective optimization of geometry of staggered herringbone micromixer *Microfluid. Nanofluid.* **7** 29–43
[53] Cortes-Quiroz C A, Azarbadegan A, Zangeneh M and Goto A 2010 Analysis and multi-criteria design optimization of geometric characteristics of grooved micromixer *Chem. Eng. J.* **160** 852–64
[54] Gomez-Aranzadi M, Arana S, Mujika M and Hansford D 2015 Integrated microstructures to improve surface-sample interaction in planar biosensors *IEEE Sens. J.* **15** 1216–23
[55] Mott D R, Obenschain K S, Howell P B and Oran E S 2008 Designing microfluidic components for enhanced surface delivery using a genetic algorithm search *46th AIAA Aerospace Sciences Meeting and Exhibit* (Reston, VA: American Institute of Aeronautics and Astronautics)
[56] Lynn N S, Šípová H, Adam P and Homola J 2013 Enhancement of affinity-based biosensors: effect of sensing chamber geometry on sensitivity *Lab Chip* **13** 1413–21
[57] Lynn N S, Martínez-López J I, Bocková M, Adam P, Coello V, Siller H R and Homola J 2014 Biosensing enhancement using passive mixing structures for microarray-based sensors *Biosens. Bioelectron.* **54** 506–14
[58] Lynn N S and Homola J 2015 Biosensor enhancement using grooved micromixers: part I, numerical studies *Anal. Chem.* **87** 5516–23
[59] Lynn N S, Bocková M, Adam P and Homola J 2015 Biosensor enhancement using grooved micromixers: part II, experimental studies *Anal. Chem.* **87** 5524–30
[60] Jain M, Rao A and Nandakumar K 2013 Numerical study on shape optimization of groove micromixers *Microfluid. Nanofluid.* **15** 689–99
[61] Kamholz A E and Yager P 2001 Theoretical analysis of molecular diffusion in pressure-driven laminar flow in microfluidic channels *Biophys. J.* **80** 155–60
[62] Kamholz A E and Yager P 2002 Molecular diffusive scaling laws in pressure-driven microfluidic channels: deviation from one-dimensional Einstein approximations *Sensors Actuators* B **82** 117–21
[63] Casalini T, Salvalaglio M, Perale G, Masi M and Cavallotti C 2011 Diffusion and aggregation of sodium fluorescein in aqueous solutions *J. Phys. Chem.* B **115** 12896–904
[64] Galambos P and Forster F K 1998 Micro-fluidic diffusion coefficient measurement *Micro Total Analysis Systems '98* pp 189–92 (Berlin: Springer)
[65] Saltzman W M, Radomsky M L, Whaley K J and Cone R A 1994 Antibody diffusion in human cervical mucus *Biophys. J.* **66** 508–15
[66] Forbes T P and Kralj J G 2012 Engineering and analysis of surface interactions in a microfluidic herringbone micromixer *Lab Chip* **12** 2634–7
[67] Hossain S, Ansari M A and Kim K Y 2009 Evaluation of the mixing performance of three passive micromixers *Chem. Eng. J.* **150** 492–501
[68] Raza W, Hossain S and Kim K Y 2020 A review of passive micromixers with a comparative analysis *Micromachines* **11** 455